RESEARCH ARTICLE

Key Points:
- Magnetic domain wall pinning at dislocations is readily observable in TEM
- Dislocation length and density affect how strongly domain walls are pinned
- Changes in coercivity from deformation are measurable using FORC diagrams

Supporting Information:
- Readme
- Video S1
- Video S2

Correspondence to:
A. K. Lindquist,
alindq@uark.edu

Domain wall pinning and dislocations: Investigating magnetite deformed under conditions analogous to nature using transmission electron microscopy

A. K. Lindquist[1], J. M. Feinberg[1], R. J. Harrison[2], J. C. Loudon[3], and A. J. Newell[4]

[1]Institute for Rock Magnetism, Department of Earth Sciences, University of Minnesota, Twin Cities, Minneapolis, Minnesota, USA, [2]Department of Earth Sciences, University of Cambridge, Cambridge, UK, [3]Electron Microscopy Group, Department of Materials Science and Metallurgy, University of Cambridge, Cambridge, UK, [4]Marine, Earth and Atmospheric Sciences, North Carolina State University at Raleigh, Raleigh, North Carolina, USA

Abstract In this study, we deformed samples cut from a single magnetite octahedron and used transmission electron microscopy (TEM) and magnetic measurements to experimentally verify earlier computational models of magnetic domain wall pinning by dislocations and to better understand the nature of dislocations in magnetite. Dislocations in magnetite have been of interest for many decades because they are often cited as a likely source of stable thermoremanent magnetizations in larger multidomain (MD) magnetite grains, so a better understanding of dislocation effects on coercivity in MD magnetite is crucial. TEM imaging shows, for the first time, domain walls sweeping through the magnetite sample and being pinned at dislocations. In agreement with theory, these findings demonstrate that domain walls are more strongly pinned at networks of dislocations than at single dislocations and that domain walls pinned at longer dislocations have higher microcoercivities than those pinned at shorter dislocations. This experimentally illustrates the ability of dislocations to increase the coercivity of larger multidomain magnetite grains. The observed values for microcoercivity and bulk coercivity are in reasonable agreement with theoretical calculations. Burgers vectors were determined for some dislocations to verify that they were in keeping with expected dislocation orientations. The dislocations were found to be primarily located on close-packed {111} planes within the magnetite. Deformation caused only a minor change in bulk coercivity, but first-order reversal curve diagrams show populations with increased coercivity not visible in hysteresis loops.

1. Introduction

Magnetite (Fe_3O_4) is ubiquitous in nature, and researchers often rely on the magnetic record preserved by magnetite when investigating geomagnetic field variations [*Cox*, 1969; *Tric et al.*, 1992; *Tauxe*, 1993; *Klitgord*, 1976]. Its ability to carry a magnetic remanence is grain size dependent. The smallest grains (<30 nm [*Dunlop*, 1973]) are superparamagnetic and cannot carry a remanence because thermal fluctuations randomize their magnetic moments [*Dunlop and Özdemir*, 1997, p. 132]. Larger grains can carry a magnetic remanence, but the domain state varies with grain size and shape. The smallest remanence-carrying grains are single domain (SD), meaning the magnetization within the grain is nearly uniform. If a grain has a nonellipsoidal shape, there are small deflections of the magnetization toward features like edges. This state, called the "flower" state [*Schabes and Bertram*, 1988] is a generalized SD state, and despite the magnetic deflections, this state is nearly saturated [*Newell and Merrill*, 1998]. The SD state has the largest magnetic moment per unit mass and also the largest coercivity of remanence. Thus, SD grains can retain a magnetic recording of Earth's magnetic field orientation that is stable over hundreds of millions of years.

In grains whose long axis ranges from 80 nm (for small aspect ratios) to over 300 nm (for large aspect ratios) [*Newell and Merrill*, 1999; *Witt et al.*, 2005], the SD state becomes unstable and vortex states form [*Schabes and Bertram*, 1988]. Vortex states have a circular arrangement of spins that reduces the magnetostatic energy and the magnetic moment; they are less efficient carriers of magnetic remanence.

For still larger grain sizes, the vortex state resolves into discrete, uniformly magnetized regions called domains. These domains are separated by relatively narrow domain walls, wherein the magnetization rotates from alignment with one domain to alignment with the neighboring domain. This domain state is

called multidomain (MD), while the transition between SD and MD is generally called pseudo-single domain (PSD) in the paleomagnetic community. Depending on how PSD behavior is defined, estimates of its upper size limit range from 3 μm [*Worm and Markert*, 1987] to 100 μm [*Heider et al.*, 1992].

In defect-free MD grains, these magnetic domain walls sweep readily through the magnetite, making it easy to alter the sample's magnetization with very low applied fields. Variations in the strength of the Earth's magnetic field (which usually ranges from 0.05 to 0.2 mT) or its orientation would be more than sufficient to remagnetize these MD grains. This behavior also makes it difficult for such grains to retain a geologically meaningful magnetic remanence because they revert back to an equilibrium state with no net magnetization once a magnetic field is removed.

A simple physical model to explain and predict the acquisition of thermoremanent magnetization (TRM) in SD grains of magnetite is one of the major accomplishments of the rock magnetic community [*Neel*, 1949]. However, PSD and MD magnetite, though common in nature, pose serious problems for many paleomagnetic applications because their remanence acquisition processes are not well understood. As a result, paleomagnetists expend a great deal of effort looking for natural materials that contain a significant fraction of SD grains (e.g., seafloor basaltic glass and silicate-hosted inclusions). They then use laboratory techniques (e.g., alternating field or low-temperature demagnetization) to minimize the remanence associated with these larger, poorly understood grains.

Unfortunately, PSD and MD grains dominate most natural rock samples. Understanding the processes that determine the remanent magnetizations in such nonideal grains is an important step toward the use of these grains in paleomagnetic applications. Earlier studies have posited that MD magnetite can have higher coercivities and retain a magnetization over geologic timescales if the domain walls are pinned by crystallographic imperfections such as dislocations, inclusions, or void spaces [*Özdemir and Dunlop*, 1997; *Moskowitz*, 1993b]; even externally applied stresses have been shown to alter domain structures [*Appel and Soffel*, 1984]. The ability of dislocations to pin domain walls has been further suggested from experimental work on bulk samples by comparing the coercivity of low-stress hydrothermally grown magnetite to that of equivalently sized high-stress mechanically ground magnetite [*Özdemir and Dunlop*, 1997].

Stacey and Wise [1967] first modeled the interactions between a single edge dislocation and a parallel domain wall, deriving an equation for the field necessary to unpin a domain wall from a dislocation. Because the calculated unpinning field was significantly smaller than the measured coercivity for their sample, they hypothesized that networks of dislocations would be necessary to explain the elevated measured coercivities of some MD magnetite samples. Later, *Xu and Merrill* [1989, 1990] would build on this work by deriving equations for screw dislocations, using the term "microcoercivity" for the field required to unpin a domain wall from a single dislocation. They also derived an equation for the bulk coercivity of a grain that is a function of microcoercivity, dislocation density, and saturation magnetization. *Hodych* [1982] investigated the relationship between coercivity and magnetostriction on powdered magnetite samples and found that the coercivity of MD magnetite was likely controlled by internal stress. *Moskowitz* [1993b] analytically determined the effects of temperature on microcoercivity for a variety of simple dislocation structures. Together, these models can be used to calculate approximate pinning fields generated by individual dislocations and dislocation pairs. However, these models have never been verified by direct imaging of domain wall interactions with dislocations.

Magnetite has an inverse spinel structure where the oxygen anions form a face-centered cubic (fcc) sublattice. This lattice creates tetrahedral sites, some of which contain Fe^{3+} cations, and octahedral sites, which may contain Fe^{2+} or Fe^{3+} cations. To accommodate the iron cations, the oxygen lattice is slightly distorted [*Dunlop and Özdemir*, 1997, pp. 48–49]. In a perfect monatomic fcc lattice, the preferred directions for the Burgers vector (representations of the magnitude and direction of the lattice displacement from a dislocation) are the ⟨110⟩ directions because they are the shortest lattice vectors (the energy of a dislocation is proportional to the square of the magnitude of the Burgers vector). The {111} planes in magnetite are parallel to layers of close-packed oxygen atoms, so less energy is required for dislocations to move along these planes. Therefore, slip is often expected to occur in the close-packed {111} glide planes [*Hornstra*, 1960]. Partial dislocations (Shockley and Frank) can also occur in magnetite; Burgers vectors in ⟨112⟩ directions would be expected for these [*Hull and Bacon*, 1984]. Partial dislocations occur when a dislocation is dissociated into parts, which have shorter Burgers vectors.
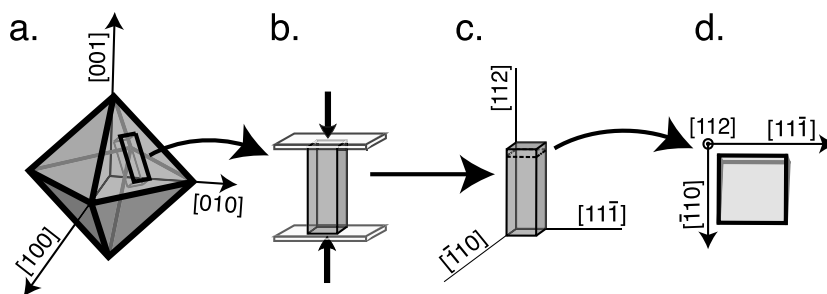
Figure 1. Schematic diagram of sample preparation. All five samples started as a single magnetite octahedron. It was cut into eight pieces, four of which were deformed and one of which was used as a control sample. Slices were cut from each bar of magnetite (after deformation, if applicable) and wedge polished to make TEM specimens.

There are few observations of dislocation geometry in magnetite itself. *Charpentier et al.* [1968] investigated glide planes, the crystallographic planes along which dislocations most easily move, in magnetite using microhardness indentation tests. They reported that both the {111} and the {100} glide planes are active at room temperature. *Heider et al.* [1987] counted dislocation densities in hydrothermally grown magnetite crystals using etch pits but did not characterize the dislocation geometry. In one of the few TEM investigations of dislocations in magnetite, *Banfield et al.* [1994] imaged the microstructures found in a lodestone consisting of magnetite, maghemite, and minor amounts of hematite, goethite, and clinopyroxene. Magnetite-maghemite intergrowths contained planar faults parallel to {101} and demonstrated a decrease in coercivity after heating, likely due to the annealing out of some microstructures. Unfortunately, the complex exsolution fabric within this lodestone specimen makes it difficult to extrapolate its dislocation structures to pure magnetite crystals.

Recent advances in large-scale computational dislocation models [*Bulatov et al.*, 2006; *Tang et al.*, 2006] may soon make it possible to numerically model complex dislocation structures in magnetite. To ensure that these dislocation models are as accurate as possible, there is a need for observations to constrain the orientation and crystallographic nature of dislocations in magnetite and to observe the interactions between these dislocations and domain walls.

This study addresses possible mechanisms of a stable TRM in MD magnetite by combining transmission electron microscopy (TEM) and bulk magnetic measurements on a suite of deformed magnetite samples. In an effort to experimentally test earlier analytical studies on domain wall pinning at dislocations, we imaged the interactions between the dislocations and magnetic domain walls. A TEM can be used to determine the Burgers vector, line direction, and character (edge, screw, or mixed) of a dislocation. A TEM can also image magnetic structures, like domain walls, when operated in Lorentz mode [*Kasama et al.*, 2010]. The effects of dislocations on domain wall motion can then be observed. We assess the retention of a magnetic recording in MD magnetite containing dislocations using magnetic hysteresis loops and first-order reversal curve (FORC) diagrams. To ensure that the magnetite samples contained dislocations, they were each deformed uniaxially to varying degrees at temperature and pressure conditions consistent with natural tectonic settings; some of the dislocations were characterized. A better understanding of domain wall and dislocation interactions can be used to help develop new generations of micromagnetic models that include the three-dimensional nature of dislocation networks, bringing researchers closer to achieving the goal of *Dunlop* [1965], where "the ultimate aim of theoretical rock magnetism is to be able to predict the magnetic behavior of any rock sample."

2. Methods

A single magnetite octahedron was cut into eight rectangular rods approximately 2.5 by 2.5 by 8 mm. The [112] direction is parallel to the long axis of each sample. A more complete crystallographic description of the samples is shown in Figure 1.

The samples will be referenced as DS0, DS0', DS1, DS2, DS3, and DS4. DS0 was neither heated nor exposed to external stresses. DS0' was not exposed to external stresses but was heated to 875°C for 72 h in an atmosphere that was 95% CO_2 and 5% CO. The same atmosphere was used for the deformed samples. DS1,

Table 1. Sample Descriptions[a]

| | T | P | t | $\dot{\varepsilon}$ | ρ | H_c | M_r | M_s |
	(°C)	(MPa)	(h)	(10^{-9} 1/s)	(10^{10} 1/m^2)	(mT)	(Am^2/kg)	(Am^2/kg)
DS0	na	na	na	na	0.84 ± 0.16	0.29	0.157	93.5
DS0′	875	0	72	na	na	na	na	na
DS1	1011	50.6	24	91 ± 2	1.3 ± 0.56	0.36	0.334	92.7
DS2	853	38	67	3.4 ± 3.0	11 ± 6.2	0.53	0.466	103
DS3	989	19.8	69	2.6 ± 1.8	4.2 ± 2.5	0.36	0.427	91.5
DS4	705	50.3	120	1.3 ± 1.3	21 ± 10	0.37	0.189	92.8

[a]Summary of deformation conditions, resulting strain rate, dislocation density, and hysteresis values for each sample. DS0 is the undeformed sample; DS0′ is the undeformed sample after heating only. T is temperature, P is pressure, t is time, $\dot{\varepsilon}$ is strain rate, ρ is dislocation density, H_c is coercivity, M_r is magnetic remanence, and M_s is the saturation magnetization. Not available = na.

DS2, DS3, and DS4 were deformed in the lab, each at unique temperature and pressure conditions. They were then investigated using magnetic measurements and TEM imaging. When not in use, the magnetite samples were stored in a vacuum box with desiccant to minimize alteration and oxidation along sample surfaces.

2.1. Deformation Experiments

Magnetite rods were deformed using a one-atmosphere rig, which operates with one atmosphere of confining pressure, and a Eurotherm furnace. The atmosphere in the chamber was kept at a mixture of 95% CO_2 and 5% CO to prevent oxidation of samples [*Hayes and Grieveson*, 1981]. A direct current displacement transducer (DCDT) was used to measure the change in sample length over the course of the experiment, and a type R thermocouple was used to measure the temperature. The samples deformed at relatively slow rates, making it difficult for the DCDT to accurately measure the change in sample length and causing some of the high error values in Table 1.

Samples were placed between two Y-stabilized ZrO_2 plates (Figure 1b) in an enclosed chamber. After heating the chamber to the desired temperature, weights were added to apply stress to the sample. The cross section of the sample was measured and used to calculate the amount of mass needed to create the desired stress. Stress was applied parallel to the magnetite [112] axis. Temperature and pressure conditions were selected to be within the dislocation creep regime as recently calculated by *Till and Moskowitz* [2013]. This deformation mechanism map addresses problems with the values for oxygen diffusion used in earlier maps [*Crouch and Robertson*, 1990; *Atkinson*, 1977]. Deforming the magnetite samples in the dislocation creep regime was ideal for three reasons. First, these conditions are similar to deformation conditions observed in natural magnetite [*Housen et al.*, 1995]; second, strain rate in this regime is grain size independent; and third, the capabilities of the apparatus used for the experiments fell within the conditions necessary for deformation in this regime.

Experimental parameters for each of the four deformation experiments are listed in Table 1. Samples deformed at lower strain rates were allowed to run for longer periods of time than those deformed at higher strain rates, ensuring they had adequate time to develop deformation microstructures. The cooling of the samples to room temperature varied between experiments. DS1 was cooled to about 800°C at approximately 150°C/h before removing the applied stress and continuing to cool at the same rate to room temperature. DS2 and DS3 were cooled to approximately 450°C at 250°C/h before removing the weights then cooled to room temperature in two more hours. DS4 was cooled from 705°C to 650°C in half an hour. The weights were then removed, and it cooled to room temperature in about 2 h. By cooling the samples rather quickly, we hoped to minimize any annealing.

2.2. TEM Imaging and Sample Preparation

To prepare samples for transmission electron microscopy (TEM) imaging, slices were cut from the magnetite rod using a small rock saw with a diamond blade. They were then polished following the technique outlined in *Voyles et al.* [2003], with the primary deviation being that after wedge polishing on diamond lapping films, samples were ion milled to remove any remaining sample roughness and to obtain the desired thinness for

electron transparency (∼100 nm). The TEM samples were then imaged on a Tecnai T12 microscope, operated at 120 kV, in the Characterization Facility at the University of Minnesota and on a Philips CM300, operated at 300 kV, at the University of Cambridge. Both TEMs were equipped with CCD cameras. The Philips CM300 is also equipped with Ditabis imaging plates and a video output that was converted from analog to digital and recorded by a computer.

The Burgers vectors of some dislocations were characterized using diffraction contrast imaging [*Howie and Whelan*, 1962]. A dislocation will not be visible in a TEM image if the following criterion is met:

$$\mathbf{g} \cdot \mathbf{b} \times \mathbf{u} = 0 \qquad (1)$$

For these equations, $\mathbf{u}$ is the unit vector along the line of the dislocation, which can be determined from TEM images, and $\mathbf{b}$ is the Burgers vector of the dislocation. The reciprocal lattice vector, $\mathbf{g}$, represents the electrons diffracted off a single crystallographic plane.

Darkfield images are created using only electrons that have been diffracted off of a single crystallographic plane within the sample (called $\mathbf{g}$). Then, by finding two darkfield images in which the dislocation is not visible (in other words, two values of $\mathbf{g}$ for which $\mathbf{g} \cdot \mathbf{b} = 0$), it is possible to solve for $\mathbf{b}$. Once the Burgers vectors are determined, finding the nature of the dislocations (edge, screw, and mixed) is simply a matter of comparing the orientation of the Burgers vector to that of the dislocation itself. Edge dislocations are perpendicular to their Burgers vector, screw dislocations are parallel, and mixed dislocations are neither.

2.3. Lorentz Imaging in Transmission Electron Microscopy

In traditional transmission electron microscopy, a sample is placed immediately adjacent to the objective lens. This lens generates a large (∼2 T) magnetic field oriented along the axis of the microscope which saturates the magnetization of the sample, driving domain walls out of multidomain grains and making imaging of magnetic structures difficult, if not impossible. The Lorentz mode of transmission electron microscopy makes imaging of domain walls possible by removing this magnetic field. An additional lens, the Lorentz lens, is installed below the objective lens and far from the sample and performs the work normally done by an objective lens, focusing the image after the electrons have passed through the sample. The objective lens can then be turned off, meaning the sample is in a low-field region of the TEM. In this way, it becomes possible to image the domain walls in the TEM without magnetically saturating the sample. There are two types of Lorentz microscopy, Fresnel and Foucault. In Fresnel imaging, magnetic domain walls appear as bright or dark lines; in Foucault imaging each magnetic domain is bright or dark, depending on the orientation of its magnetization. Because Fresnel imaging highlights the domain walls but does not affect the rest of the TEM image, it was selected for this study. Both types of imaging utilize the deflection of the electron beam due to Lorentz forces as it passes through a magnetic sample. Electrons passing through different magnetic domains within the sample will be deflected in different directions based on the magnetization of that domain. When images are collected at the focal plane, this deflection is not visible. However, in the Fresnel imaging mode the image is slightly overfocused or underfocused—typically by about 1 mm. Wherever domain walls are present, electrons will be deflected to converge or diverge, creating bright or dark lines. The contrast (dark or light) of a domain wall in a Fresnel image will change depending on whether the image was collected above or below the focal plane.

The imaging done in this study uses the same principles, but without a Lorentz lens. Instead, the microscope was operated in low-magnification mode, with the objective lens turned off, and the diffraction lens was used to focus the image. A small 16.8 mT vertical field oriented parallel to the axis of the microscope remained in the vicinity of the sample. By tilting the sample, it was possible to change the in-plane magnetization of the sample from 0 to 16.8 mT and observe the resulting domain wall motion. Lorentz imaging was done on the Philips CM300 TEM at the University of Cambridge.

2.4. Magnetic Measurements

Hysteresis loops were measured at the Institute for Rock Magnetism (IRM) at the University of Minnesota using a MicroMag Princeton Measurements Corporation vibrating sample magnetometer (VSM). The hysteresis loops were measured using fields up to 1.0 T. Multiple loops were measured for each sample at different times to ensure consistency and repeatability.
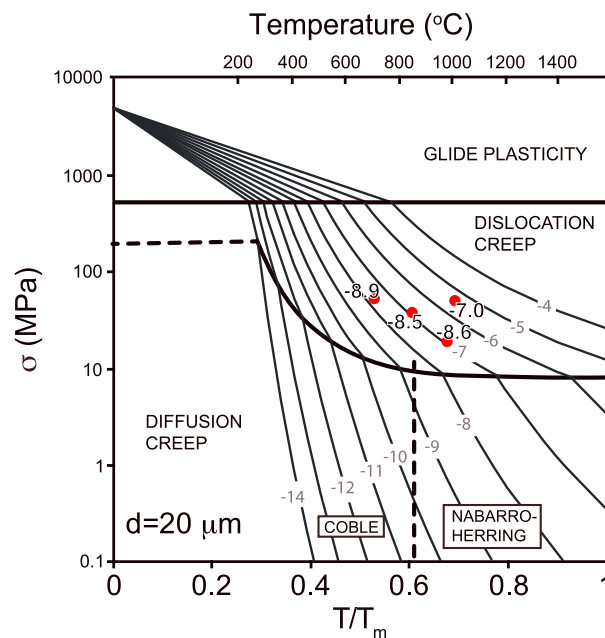
Figure 2. Deformation mechanism map for magnetite with points indicating deformation conditions for samples DS1–DS4. The vertical axis represents applied stress; the horizontal axis is temperature with T/T_m representing the ratio of deformation temperature to the melting point of magnetite ($T_m = 1538°C$). The measured strain exponent for each experiment is listed alongside its corresponding dot and differs from the expected value by 1 to 2 orders of magnitude. Figure adapted from *Till and Moskowitz* [2013].

First-order reversal curve (FORC) measurements were conducted on 3 to 5 mg pieces at room temperature using a MicroMag Princeton Measurements Corporation VSM at the Institute for Rock Magnetism (IRM) at the University of Minnesota. The FORC diagrams were calculated using the VARIFORC (VARIable FORC smoothing) method [*Egli*, 2013] in the FORCinel software [*Harrison and Feinberg*, 2008]. FORC diagrams are useful because they provide an in-depth look at the distribution of the microcoercivities within a sample, thereby allowing one to see the range of stability with which a sample will retain a magnetic recording.

2.5. Dislocation Density Estimates
To quantify the distribution of deformation within the magnetite samples and to estimate the concentration of dislocations within each magnetite sample, etch pit studies were carried out. A piece was cut from the magnetite samples and placed in 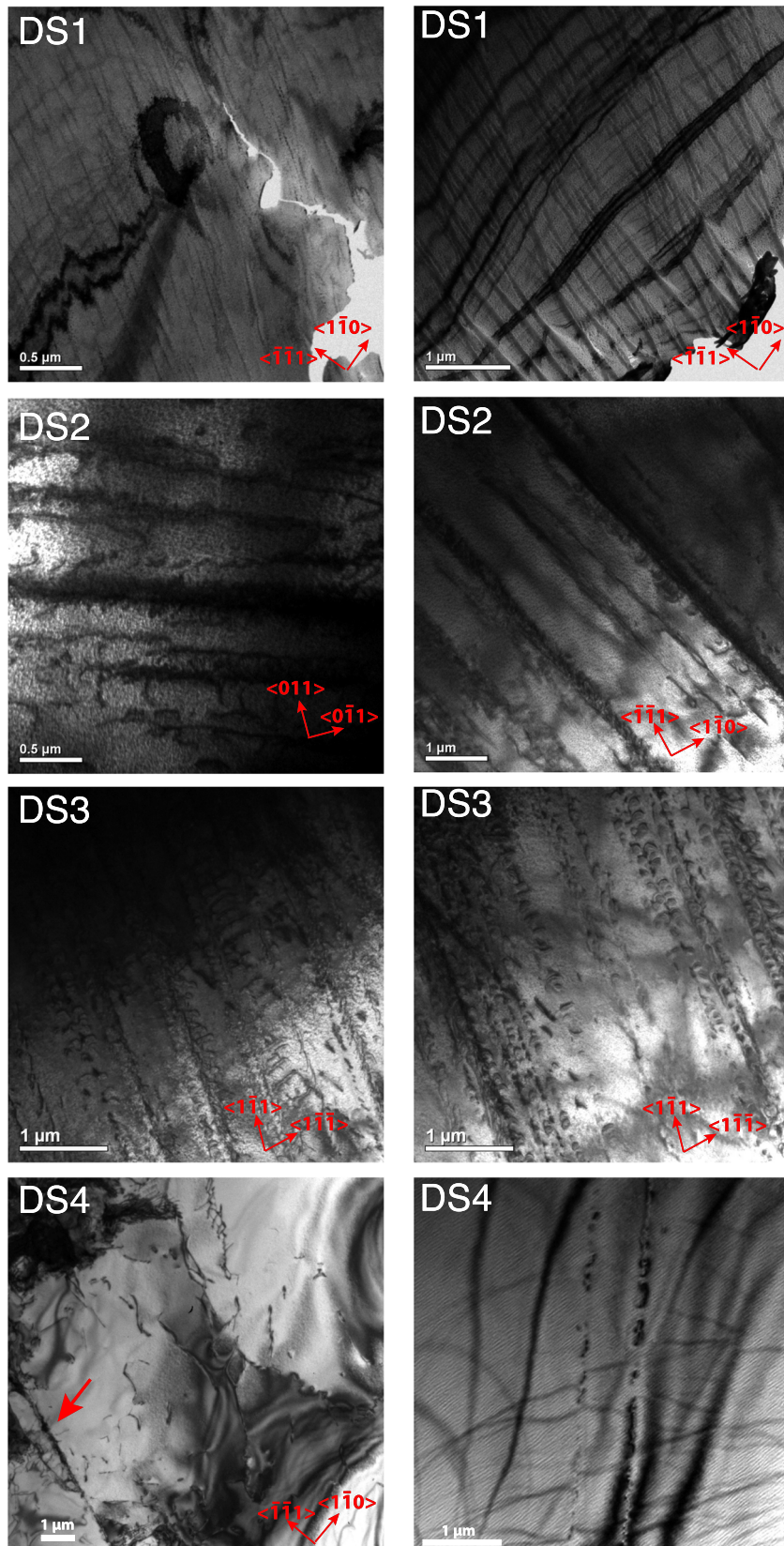concentrated hydrochloric acid for 10–15 s [*Heider et al.*, 1987] before being quickly rinsed. Samples were then imaged using a Hitachi table-top scanning electron microscope (SEM) to determine dislocation densities. Approximate dislocation densities were obtained by counting the number of triangular dislocation etch pits in a series of images and averaging these counts to find dislocation density (in $1/m^2$).

3. Results
3.1. Deformation
Strain rates for each of the five experiments are shown in Table 1 and are plotted on the deformation mechanism map in Figure 2. All four of the deformation experiments plot within the dislocation creep regime. The experimental strain rate is up to 2 orders of magnitude lower than predicted from the deformation mechanism map. This is believed to be the result of two factors: (1) difficulties calculating the rate of change in length, because of the relatively short experiment duration and the high amount of noise in the measured rate of shortening values, and (2) the fact that the magnetite appears to have deformed in concentrated bands instead of uniformly throughout the sample.

3.2. Microstructures
Deformation microstructures were present in all deformed samples, though the type and arrangement of these microstructures differed between samples. Examples of deformation microstructures from each sample are shown in Figure 3. Four to eight dislocations were characterized per sample. These results are discussed below. Though not readily visible in the TEM images, it is important to note that the dislocations were not uniformly distributed throughout the samples. Sample DS1 is the only sample with obvious deformation bands. They are the primary feature in TEM images and are visible as slightly darker bands running NE to SW within the sample.

A deformation band is a planar region whose crystallographic orientation is distinctly different from the surrounding area [*Kuhlmann-Wilsdorf*, 1999; *Zhang et al.*, 2001]. Deformation bands are broader than dislocations and tend to form parallel to the easy slip planes [*Higashida et al.*, 1986]. They are more common

Figure 3. TEM images showing microstructures in deformed samples. The arrow indicates a possible subgrain created during deformation of DS4.
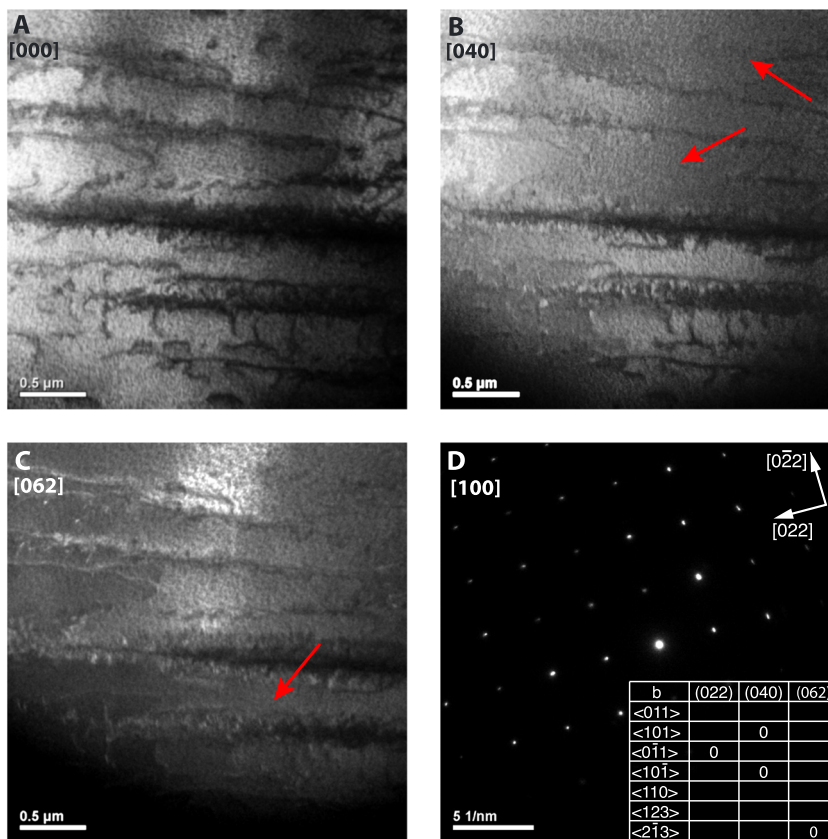
Figure 4. (a) Bright-field image collected using electrons from the undefracted spot, (b and c) darkfield images collected from the labeled planes, and (d) a diffraction pattern corresponding to the images. The inset table illustrates part of a sample calculation of the Burgers vector of a dislocation. The arrows highlight regions in which dislocations are not visible in the darkfield images but are present in the bright-field image.

in larger grains than in smaller ones, and they can range in size from a few unit cells in width to nearly 3 mm, depending on the sample [*Kuhlmann-Wilsdorf et al.*, 1999]. The deformation bands in these samples are on the smaller end of this spectrum, with widths around 0.1 μm. There were often slight variations in diffraction patterns as a result of the differing crystallographic orientations at deformation bands. In DS1 the alignment of the deformation bands primarily coincides with the [$\bar{1}11$] direction in the sample (Figure 3), which is consistent with the slip planes proposed by *Hornstra* [1960]. Dark bands running through the sample, roughly parallel to the sample's edge, are thickness fringes.

In samples DS2 and DS3 dislocations appear to be concentrated in bands or planes and are primarily linear or short arcs (Figure 3). Those characterized were primarily mixed instead of being pure screw or edge dislocations, though some appear to contain regions that are purely screw dislocations. Most of the characterized Burgers vectors are in the expected $\langle 110 \rangle$ directions, but a few are in the $\langle 123 \rangle$ and $\langle 112 \rangle$ directions. Dislocation buildups appear to occur in the $\{111\}$ planes and may be precursors to eventual deformation band formation. Figure 4 contains images of dislocations found in sample DS2 and shows examples of dislocation extinction along the appropriate darkfield orientations. The inset table is a sample of a table used for determining the Burgers vectors of the dislocations.

Sample DS4 has a higher dislocation density than the other samples and is also notable because it was deformed at the lowest temperature. In DS4, dislocation structures are more complex (Figure 3), and in some regions subgrain boundaries have formed, causing slight variations in the crystallographic orientation of the magnetite within dislocation-rich regions. The dislocations here primarily have Burgers vectors with $\langle 110 \rangle$ orientations and are mixed in nature.

Energy dispersive X-ray spectroscopy (EDS) was used to characterize the composition of the samples, which was found to be nearly pure magnetite. The measured average atomic percent of iron and of oxygen are
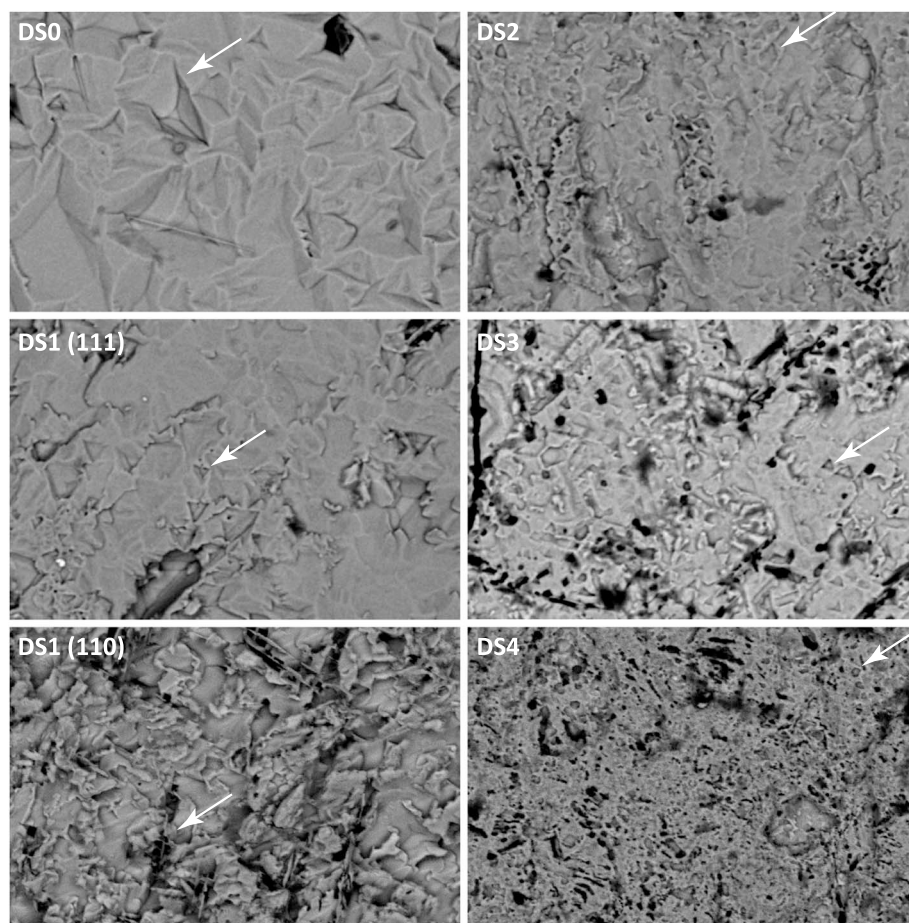
Figure 5. SEM images of etch pits on all five samples. All images are 50 μm by 75 μm. If unlabeled, the (111) face is shown. As in *Heider et al.* [1987], a one to one correlation is assumed between etch pits (triangular pits on surface of crystal) and total dislocations within the sample. For each image, one triangular etch pit is indicated with an arrow, though many are present in each image. In DS1 (110), a longer series of etch pits is indicated. This may be illustrative of a deformation band intersecting the surface of the crystal.

57.7 ± 0.7% and 42.4 ± 0.5%, respectively. Pure magnetite contains 57.1% Fe and 42.9% O. No other cations were observed with EDS to have atomic abundances higher than 0.5%, the detection limit of the EDS.

Etch pits (Figure 5) were used to approximate the dislocation density for each sample and were counted using SEM images. The average dislocation density for each sample is reported in Table 1. The distribution of values is centered around 10^{10} m^{-2}, which is in good agreement with natural samples [*Soffel*, 1969; *Heider et al.*, 1987]. Etch pit counts were highest for sample DS4 and lowest for DS1. Short, linear collections of etch pits were visible in samples DS1 and DS3. These are believed to indicate deformation bands intersecting the surface of the grain. In all samples, etch pit observations suggested that dislocations were concentrated in wide, linear clusters instead of being uniformly distributed throughout the sample. Rather, deformation was greater in some regions than others, as evidenced by bands with higher dislocation concentrations than the surrounding crystal. The dislocation density values were calculated over large enough areas to incorporate this variability. In the undeformed sample, dislocation densities are sufficiently low that it is unlikely they would be observed during a TEM analysis [*Morrison-Smith et al.*, 1976].

3.3. Domain Wall Observations

Magnetic images from Lorentz-mode TEM imaging were only obtained for sample DS4. The magnetite sample was tilted within the TEM to vary the in-plane magnetic field, causing the domain walls to move. When tilting the sample, it was possible to see domain walls becoming pinned along dislocations (Videos S1 and S2 in the supporting information and Figures 6 and 7). Domain walls appear to preferentially pin along the length of dislocations instead of transecting them. This is especially evident in Video S2 where
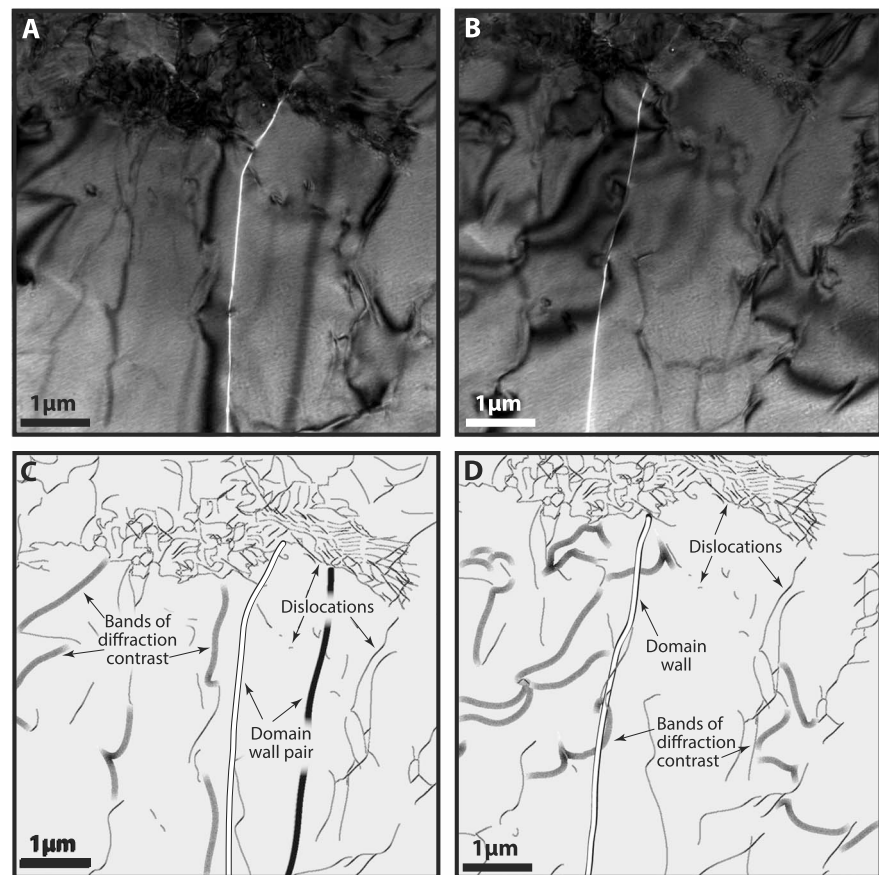
Figure 6. Lorentz imaging of the same magnetic domain wall in different locations. Imaging above or below the focal plane changes the contrast of the domain wall from dark to light. This property is responsible for the difference in contrast in the domain wall between Figures 6a and 6b. (a and b) The domain wall pins at some of the short dislocations arranged in linear dislocation networks as it is forced to migrate through the imaging plane by tilting the sample and changing the in-plane magnetization. (c and d) Schematic diagrams for Figures 6a and 6b. The domain wall in Figure 6b is indicated with an arrow. Though the domain wall is not aligned along the dislocations in this figure, there are instances in the corresponding Video S1 where it is largely aligned along one of these linear dislocation features. However, because these features are made up of many short dislocations (which do not pin as strongly as long dislocations) and because of additional forces from the changing magnetic field and other nearby dislocations, the domain wall is not always aligned along the two linear dislocation features.

the domain wall can be seen jumping in a stick-slip pattern from one dislocation to another. Video S1 shows Barkhausen jumps, instances where domain walls become unpinned, occurring at an average interval of 0.12 ± 0.04 mT. Video S2 shows stronger pinning behavior, with unpinning requiring average fields of 0.27 ± 0.06 mT. Figures 6 and 7 illustrate domain wall pinning at dislocations in magnetite. The dislocations in both videos were difficult to see consistently throughout tilting experiments, so to help the reader, lines have been added to make them recognizable. The two linear features visible in Video S1 and Figure 6 are actually a network of shorter dislocations but were highlighted with two lines for ease of viewing. Figure 7 helps to illustrate the positions of a domain wall from Video S2 as it moves through the region of interest, highlighting the tendency of the domain walls to hop from dislocation to dislocation as they progressively migrate across a sample.

3.4. Magnetic Measurements

Major hysteresis loops are very similar between samples (Table 1). Bulk coercivities and remanence magnetization show minor increases with deformation but vary only slightly between samples. The saturation magnetization of sample DS2 was slightly larger than that of the other samples. Some of the variation in magnetic remanence between samples is the result of collecting hysteresis measurements on unoriented magnetite fragments. Though not shown, hysteresis loops were also measured for DS4 along
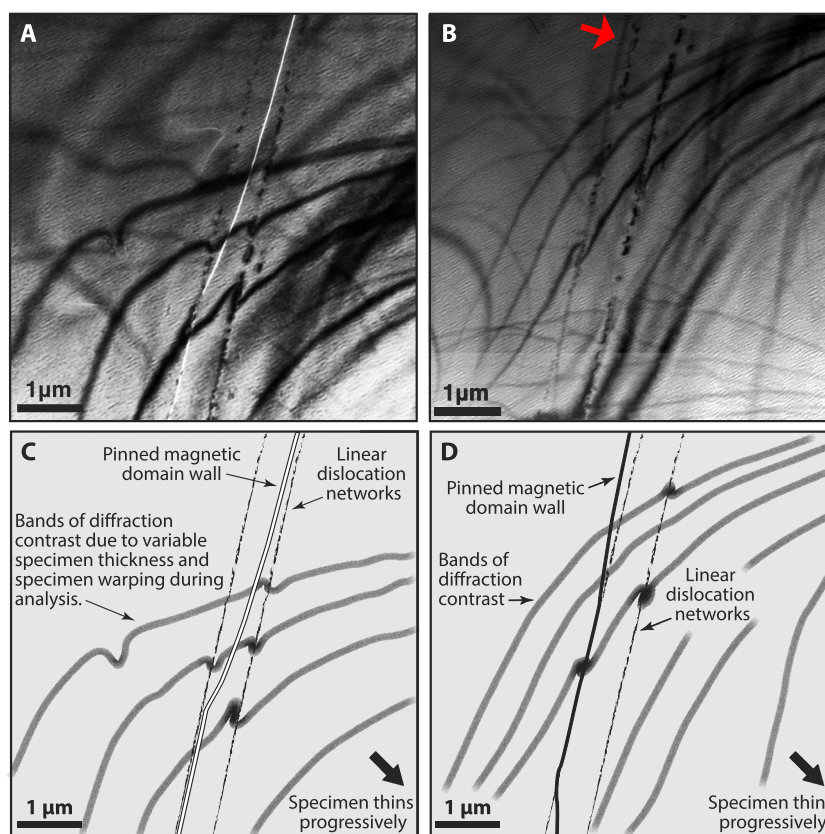
Figure 7. (a and b) TEM images showing domain walls in a field of dislocations. The domain walls bend to intersect dislocations within the magnetite sample, indicating that it is energetically preferable for them to intersect dislocations when in close proximity. (c and d) Illustrations of the regions shown in Figures 7a and 7b with relevant features indicated.

the [112], [111], and [110] axes. There was no significant difference between the saturation magnetizations (91.7–92.7 Am^2/kg) or coercivities (0.35–0.38 mT) of these loops, so they are considered comparable, despite not being measured at the same orientation.

FORC diagrams were measured to more thoroughly investigate coercivity changes that may have resulted from deformation. All diagrams display MD behavior, which is visible as the vertical band at the left of the FORC diagrams in Figure 8. An increase in the upper range of the coercivity spectrum is visible as a horizontal central ridge. These ridges indicate populations of microcoercivity values of over 100 mT that are clearly visible in DS2 and DS4 and smaller higher coercivity populations in DS1. There is a very faint ridge visible in the unheated DS0, the undeformed sample. However, a small ridge, similar to that visible in DS3, arises in the undeformed sample after heating (DS0′). Sample DS2 also contains a depressed region just below the $H_u = 0$ axis. In the past, this feature has been interpreted as indicative of single-vortex behavior [*Lappe et al.*, 2011; *Pike and Fernandez*, 1999], so it is noteworthy that similar behavior is observed here in large MD-sized grains of magnetite, though it may be the result of other factors.

4. Discussion

Dislocation creep has been both observed and calculated to be an important mechanism by which magnetite deforms in nature [*Housen et al.*, 1995; *Till and Moskowitz*, 2013], especially when in a matrix of minerals that are relatively more resistant to flow than the magnetite (e.g., plagioclase). Often, studies interested in magnetite with internal microstructures and higher internal stresses use brittle deformation (crushing) to prepare samples [e.g., *Kosterov*, 2001; *Dunlop*, 1986]. By deforming samples in the dislocation creep regime, we hope to observe dislocation structures that are more analogous to those that would form in nature.
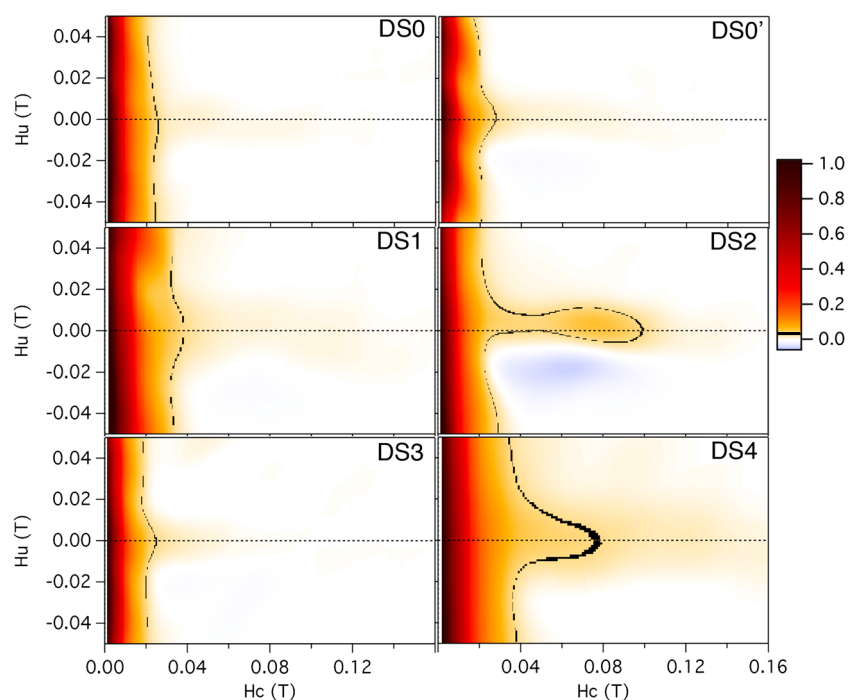
Figure 8. FORC diagrams showing coercivity distributions for all five magnetite samples. Note the differences in the central ridges along $H_u = 0$. To emphasize the extent of the coercivity spectra, a small portion of the color scale was changed to black in both the scale bar and in the corresponding region of each figure. The coercivity spectra do not reach zero until beyond this line in each figure.

4.1. Sample DS0

Sample DS0, the undeformed sample, was used as a control. Its dislocation density is below the value for which dislocations are readily visible in a TEM, 10^{10} $1/m^2$ [*Morrison-Smith et al.*, 1976], (Table 1). Further, DS0 also has the lowest coercivity of the five samples (0.29 mT).

Sample DS0' was only heated. This sample shows an increase in coercivity, despite the lack of deformation. This is likely the result of nonstoichiometry introduced during heating.

4.2. Dislocations

In order to more fully understand the effects of dislocations on the coercivity and remanence of magnetite, it is important to first discuss the dislocations themselves. The observed dislocation structures were a mix of irregular dislocation tangles (most common in DS4), isolated curves, and linear structures with arcing offshoots (most common in DS2 and DS3). As has been observed in similar studies, lower temperature deformation experiments yielded larger dislocation densities and more heterogeneous dislocation distributions [e.g., *Morrison-Smith et al.*, 1976]. At lower deformation temperatures, dislocation structures also appear to be more irregular. It is not unlikely that this is due in part to having less time for the dislocations to migrate and reach preferred orientations. As temperature increases, so does dislocation mobility, and dislocation arrangement is much more regular in DS2 and DS3. In fact, dislocation density is most closely tied to the temperature at which a sample was deformed, indicating that the increased mobility of dislocations at higher temperatures played a significant role in the development of dislocation structures. At higher temperatures (DS1 and DS3), there is more evidence for deformation bands.

In DS2 and DS3, dislocation arcs curl out from jumbles of dislocations collected along the {111} planes within the crystal. In our samples, dislocations occur primarily in {111} planes with Burgers vectors in ⟨110⟩ directions. This is typical of fcc crystals. Some dislocations had Burgers vectors in ⟨112⟩; these may be Shockley partial dislocations. In addition, a few Burgers vectors were in ⟨123⟩ directions. Dislocations were primarily mixed in character, not purely edge or screw dislocations. As predicted by *Charpentier et al.* [1968], the direction in which stress was applied had little impact on microstructure.

4.3. Microcoercivity

Calculating the in-plane magnetization of the samples while in the TEM enabled measurement of the first-ever experimental values for microcoercivity. These values were then compared to computational values of domain wall pinning at a single parallel dislocation. Pinning of domain walls along the length of a dislocation was readily observable, facilitating comparison between theory and experiment. A theoretical value for the microcoercivity, h_c, the field required to unpin a magnetic domain wall from a dislocation, was calculated using the equation for the pinning from a screw dislocation [*Xu and Merrill*, 1989] and for an edge dislocation [*Stacey and Wise*, 1967] in an infinitely large slab:

$$h_c^{\text{screw}} = \frac{1.46\mu bl\lambda_{111}}{M_s S}, \tag{2}$$

$$h_c^{\text{edge}} = \frac{0.47\mu bl(\lambda_{111} + 0.5\lambda_{100})}{M_s S}. \tag{3}$$

In these equations, μ is the shear modulus, b is the magnitude of the Burgers vector, l is the length of the dislocation, λ is the magnetostriction constant in the [111] direction or the [100] direction (as noted), M_s is the saturation magnetization, and S is the domain wall area. Equations (2) and (3) are quite similar, and the values calculated from these equations can be used to approximate pinning fields for any single dislocation. The values used in this calculation are shown in the appendix. The predicted microcoercivities, for a dislocation 1 µm long, are 0.18 and 0.67 mT for edge and screw dislocations, respectively. The observed microcoercivity of 0.27 ± 0.06 mT for a dislocation of this length (Video S2) falls within this range.

Domain walls that are pinned at shorter dislocations (Video S1) require smaller fields to overcome the dislocations than do domain walls pinned at longer dislocations (Video S2). For shorter dislocations, with lengths on the order of 0.1 µm, like those in Video S1, the calculated microcoercivities are an order of magnitude smaller, 0.018 and 0.067 mT. These values are lower than the observed value of 0.12 ± 0.04 mT. This raises the question of whether the dislocations in Video S1 may be longer than 0.1 µm.

These experimental observations agree with the previously derived theoretical microcoercivity values and provide experimental validation for both computational microcoercivities and for the relationship between increased microcoercivities and longer dislocations.

4.4. Coercivity

Understanding the coercivity of these MD magnetites is important because higher coercivities mean the samples are more likely to be able to carry a stable remanence over geologic timescales.

Hysteresis loops show a slight, but measurable, increase in the bulk coercivity of deformed samples. The dislocations and other internal structural defects are likely acting as pinning sites for domain walls, enhancing magnetic stability [*Xu and Merrill*, 1989]. FORC diagrams effectively illustrate a changing coercivity spectrum that was not otherwise visible in the hysteresis measurements. Unsurprisingly, given the size of the samples, both hysteresis loops and FORC diagrams are dominated by MD behavior [*Pike et al.*, 2001]. It is likely that this MD signal overwhelmed any minor coercivity changes, making such variability difficult to observe in standard hysteresis loops. FORC diagrams illustrate a measurable increase in coercivity with both heating and deformation. It is worth noting that—excluding DS1, which likely lost many of its dislocations due to annealing—DS2 has the highest coercivity (in hysteresis loops and FORC diagrams), remanence, and total strain.

Previously, heating of magnetite has been shown to decrease the coercivity of the sample [*Lowrie and Fuller*, 1969; *Pike et al.*, 2001] by annealing of defects. Because the defect concentrations in these samples were already low, the slight increase in coercivity visible in these FORC diagrams may be because small amounts of nonstoichiometry were introduced during heating. The FORC diagrams for the heated samples then reflect a mixture of magnetite with trace amounts of maghemite or hematite [*Muxworthy et al.*, 2005]. There is little evidence for this nonstoichiometry in other samples, so it likely had a very small impact on the samples and would not have spread to the interior of the sample, which was used for TEM imaging. The effects of this potential nonstoichiometry are relatively small and are not sufficient to cause the larger central ridges visible in the FORC diagrams for samples DS2 and DS4. This implies that something else is causing the larger central ridges visible in these samples. Because the samples did not appear fractured when imaged in the SEM, it is unlikely that fracturing would have caused this behavior.

The increase in coercivity is then likely the result of structures formed during deformation, including smaller subgrains (like the elongate region visible in sample DS4, Figure 3) and regions with high dislocation concentrations that effectively pinned domain walls.

The coercivity increase associated with dislocations can be compared to calculations of bulk coercivity using equations from *Xu and Merrill* [1990, 1992]. This calculation is especially useful for samples, like DS4, whose deformation microstructures are predominantly dislocations. Bulk coercivity, H_c, can be approximated from microcoercivity using the following relationships:

$$H_c \propto \frac{h_c^2}{M_s} \text{ (for low defect concentration)} \tag{4}$$

$$H_c = <h_c> \text{ (for high defect concentration)} \tag{5}$$

where $<h_c>$ is the mean microcoercivity, which can be approximated using the average number of defects inside a domain wall, n, via $<h_c> \approx h_c \sqrt{n}$.

Using this relationship, the experimentally measured microcoercivity value of 0.27 mT, and assuming four defects per wall (value determined using TEM images), bulk coercivity is calculated as 0.54 mT. This value is of the same order of magnitude as the coercivity values from the hysteresis loops (0.36–0.53 mT), indicating that the coercivity in these samples is likely the result of dislocation interactions with domain walls. Higher coercivities, for example, 100 mT, would require close to 150,000 dislocations per domain wall. Assuming a 100 μm long and 0.1 μm thick domain wall, this corresponds to a dislocation density on the order of 10^{15} 1/m², many orders of magnitude larger than even the most dislocation rich of the samples used in this study. This value would be smaller for longer dislocations, which pin more strongly. As can be seen in the videos, h_c can vary widely depending on the density and orientation of dislocations in a region, so it is likely that complex dislocation structures, like those seen at the left of Video S2, would be necessary for higher coercivity values.

5. Conclusions

Experimental observations verify that domain walls pin preferentially along the length of dislocations, rather than being penetrated by them. The fields required to unpin domain walls from shorter, isolated dislocations were on the order of 0.2 mT. Earth's magnetic field generally ranges from 0.05 to 0.2 mT, so at times it is strong enough to free weakly pinned domain walls. More complex dislocation structures, like those visible at the far left of Video S2, can significantly increase the strength of the pinning (in this case the domain wall remained at this dislocation structure for 2 mT). Similarly, dislocation length appears to directly influence the strength with which a domain wall is pinned, with longer dislocations pinning domain walls more strongly than shorter dislocations. In FORC diagrams, pinning fields of up to 125 mT further demonstrate that some deformation structures may enable MD magnetite to carry a stable remanence. Further investigations on pinning in regions with more complex dislocation structures may help to determine whether these higher coercivities can occur because of dislocations alone.

The dislocations in this study appear to be typical of natural magnetite and were formed at conditions analogous to those present in tectonic settings. Dislocations were found primarily in {111} planes with Burgers vectors along the ⟨110⟩ directions, but as dislocation structures became more complex, Burgers vectors were also found in ⟨123⟩ and ⟨112⟩ directions. These dislocations were observed to act as pinning sites for domain walls, increasing the coercivity of the magnetite. Both complex and simpler dislocation structures could be seen pinning domain walls to varying degrees depending on their length and their proximity to other dislocations. However, the dislocations in these samples were not uniformly distributed throughout the material. Rather, some regions were relatively dislocation free, while others contained more concentrated dislocation networks. This heterogenous distribution meant that there were large regions in which domain walls could move with relative ease. These low-coercivity regions were separated by regions with elevated coercivities in which domain walls were frequently pinned by dislocation networks. It is in these high-coercivity regions that the possibility for stable MD remanence is greatest.

Table A1. Values Used When Calculating the Microcoercivity From Theory

		Reference
μ	60.3 GPa	*Reichmann and Jacobsen* [2004]
b	4.5 Å	*Bradley et al.* [1996]
l	1 μm	estimate from images
λ_{111}	78.2×10^{-6}	*Moskowitz* [1993a]
M_s	465,750 $^A/_m$	*Domenicali* [1950]
S	10^{-11} m^2	*Xu and Merrill* [1989], sample geometry

Previous work on MD magnetite demonstrated that during TRM and pTRM acquisition the microcoercivities distributed throughout a magnetite sample are important in remanence acquisition [*Neel*, 1955; *Lowrie and Fuller*, 1971; *Dunlop and Xu*, 1994]. However, these theoretical considerations of MD TRM assume identical, evenly spaced pinning sites, which have been demonstrated to be uncommon in these deformed magnetites.

The length, density, and physical distribution of dislocations within magnetite are then all important considerations when trying to understand stable TRM acquisition and maintenance in MD magnetite. However, dislocation mobility and stress remagnetization need to also be considered. Even at room temperatures, hydrostatic stresses >100 MPa are sufficient to remagnetize magnetite grains [*Borradaile*, 1996]. Then, if using MD grains as potential recorders of Earth's magnetic field, the deformation which generates the dislocations can significantly change the remanence [*Jackson et al.*, 1993], though recent work by *Till et al.* [2010] on PSD magnetite has demonstrated that some component of the original TRM may be preserved. Further work will be necessary to better understand the remanence potential of MD magnetite.

Appendix A: Microcoercivity Calculation

When calculating the microcoercivity from theory, the following values were used.

References

Appel, E., and H. C. Soffel (1984), Model for the domain state of Ti-rich titanomagnetites, *Geophys. Res. Lett.*, *11*, 189–192.

Atkinson, B. K. (1977), The kinetics of ore deformation: Its illustration and analysis by means of deformation-mechanism maps, *Geol. Foeren. Stockholm Foerh.*, *99*, 186–197.

Banfield, J. F., P. J. Wasilewski, and D. R. Veblen (1994), TEM study of relationships between the microstructures and magnetic properties of strongly magnetized magnetite and maghemite, *Am. Mineral.*, *79*, 654–667.

Borradaile, G. J. (1996), Experimental stress remagnetization of magnetite, *Tectonophysics*, *261*, 229–248.

Bradley, J. P., R. P. Harvey, and H. Y. Jr. McSween (1996), Magnetite whiskers and platelets in ALH84001 Martian meteorite: Evidence of vapor phase growth, *Geochim. Cosmochim. Acta*, *60*(24), 5149–5155.

Bulatov, V. V., et al. (2006), Dislocation multi-junctions and strain hardening, *Nature*, *440*, 1174–1178.

Charpentier, P., P. Rabbe, and J. Manec (1968), Mise en evidence de la plasticite de la magnetite mesure de la durete en fonction de la temperature, *Mater. Res. Bull.*, *3*(2), 69–78.

Cox, A. (1969), Geomagnetic reversals, *Science*, *163*(3864), 237–245.

Crouch, A. G., and J. Robertson (1990), Creep and oxygen diffusion in magnetite, *Acta Metall. Mater.*, *38*(12), 2567–2575.

Domenicali, C. A. (1950), Magnetic and electric properties of natural and synthetic single crystals of magnetite, *Phys. Rev.*, *78*(4), 458–467.

Dunlop, D. J. (1965), Grain distributions in rocks containing single domain grains, *J. Geomagn. Geoelec.*, *17*(3–4), 459–471.

Dunlop, D. J. (1973), Superparamagnetic and single-domain threshold sizes in magnetite, *J. Geophys. Res.*, *78*(11), 1780–1793.

Dunlop, D. J. (1986), Hysteresis properties of magnetite and their dependence on particle size: A test of pseudo-single-domain remanence models, *J. Geophys. Res.*, *91*(B9), 9569–9584.

Dunlop, D. J., and Ö. Özdemir (1997), *Rock Magnetism: Fundamentals and Frontiers*, Cambridge Univ. Press, Cambridge, U. K.

Dunlop, D. J., and S. Xu (1994), Theory of partial thermoremanent magnetization in multidomain grains: 1. Repeated identical barriers to wall motion (single microcoercivity), *J. Geophys. Res.*, *99*, 9005–9023.

Egli, R. (2013), VARIFORC: An optimized protocol for the calculation of non-regular first-order reversal curve (FORC) diagrams, *Global Planet. Change*, *110*, 302–320.

Harrison, R. J., and J. M. Feinberg (2008), FORCinel: An improved algorithm for calculating first-order reversal curve distributions using locally weighted regression smoothing, *Geochem. Geophys. Geosyst.*, *9*, Q05016, doi:10.1029/2008GC001987.

Hayes, P. C., and P. Grieveson (1981), Microstructural changes on the reduction of hematite to magnetite, *Metall. Trans. B*, *12B*, 579–587.

Heider, F., D. J. Dunlop, and N. Sugiura (1987), Magnetic properties of hydrothermally recrystallized magnetite crystals, *Science*, *236*, 1287–1290.

Heider, F., D. J. Dunlop, and H. C. Soffel (1992), Low-temperature and alternating field demagnetization of saturation remanence and thermoremanence in magnetite grains (0.037 μm to 5 mm), *J. Geophys. Res.*, *97*, 9371–9381.

Higashida, K., J. Takamura, and N. Narita (1986), The formation of deformation bands in fcc crystals, *Mater. Sci. Eng.*, *81*, 239–258.

Hodych, J. P. (1982), Magnetostrictive control of coercive force in multidomain magnetite, *Nature*, *298*, 542–544.

Hornstra, J. (1960), Dislocations, stacking faults and twins in the spinel structure, *J. Phys. Chem. Solids*, *15*, 311–323.

Housen, B. A., B. A. V. D. Pluijm, and E. J. Essene (1995), Plastic behavior of magnetite and high strains obtained from magnetic fabrics in the Parry Sound shear zone, Ontario Grenville Province, *J. Struct. Geol.*, *17*(2), 265–278.

Howie, A., and M. J. Whelan (1962), Diffraction contrast of electron microscope images of crystal lattice defects: III. Results and experimental confirmation of the dynamical theory of dislocation image contrast, *Proc. R. Soc. London, Ser. A*, *262*, 206–230.

Hull, D., and D. J. Bacon (1984), *Introduction to Dislocations,* 3rd ed., Pergamon, Boston.

Jackson, M., G. Borradaile, P. Huddleston, and S. Banerjee (1993), Experimental deformation of synthetic magnetite-bearing calcite sandstones: Effects on remanence, bulk magnetic properties, and magnetic anisotropy, *J. Geophys. Res.*, *98*, 383–401.

Kasama, T., N. S. Church, J. M. Feinberg, R. E. Dunin-Borkowski, and R. J. Harrison (2010), Direct observation of ferrimagnetic/ferroelastic domain interactions in magnetite below the Verwey transition, *Earth Planet. Sci. Lett.*, *297*, 10–17.

Klitgord, K. D. (1976), Sea-floor spreading: Then central anomaly magnetization high, *Earth Planet. Sci. Lett.*, *29*(1), 201–209.

Kosterov, A. (2001), Magnetic hysteresis of pseudo-single-domain and multidomain magnetite below the Verwey transition, *Earth Planet. Sci. Lett.*, *186*(2), 245–253.

Kuhlmann-Wilsdorf, D. (1999), The theory of dislocation-based crystal plasticity, *Philos. Mag. A*, *79*(4), 955–1008.

Kuhlmann-Wilsdorf, D., J. T. Moore, E. A. Starke Jr., and S. S. Kulkarni (1999), Deformation bands, the LEDS theory, and their importance in texture development: Part I. Previous evidence and new observations, *Metall. Mater. Trans. A*, *30A*, 2491–2501.

Lappe, S.-C. L. L., N. S. Church, T. Kasama, A. B. da Silva Fanta, G. Bromiley, R. E. Dunin-Borkowski, J. M. Feinberg, S. Russell, and R. J. Harrison (2011), Mineral magnetism of dusty olivine: A credible recorder of pre-accretionary remanence, *Geochem. Geophys. Geosyst.*, *12*, Q12Z35, doi:10.1029/2011GC003811.

Lowrie, W., and M. Fuller (1969), Effect of annealing on coercive force and remanent magnetizations in magnetite, *J. Geophys. Res.*, *74*(10), 2698–2710.

Lowrie, W., and M. Fuller (1971), On the alternating field demagnetization characteristics of multidomain thermoremanent magnetization in magnetite, *J. Geophys. Res.*, *76*, 6339–6349.

Morrison-Smith, D. J., M. S. Paterson, and B. E. Hobbs (1976), An electron microscopy study of plastic deformation in single crystals of synthetic quartz, *Tectonophysics*, *33*, 43–79.

Moskowitz, B. M. (1993a), High-temperature magnetostriction of magnetite and titanomagnetites, *J. Geophys. Res.*, *98*(B1), 359–371.

Moskowitz, B. M. (1993b), Micromagnetic study of the influence of crystal defects on coercivity in magnetite, *J. Geophys. Res.*, *98*(B10), 18,011–18,026.

Muxworthy, A. R., J. G. King, and D. Heslop (2005), Assessing the ability of first-order reversal curve (FORC) diagrams to unravel complex magnetic signals, *J. Geophys. Res.*, *110*, B01105, doi:10.1029/2004JB003195.

Neel, L. (1949), Théorie du traînage magnétique des ferromagnétiques en grains fins avec applications aux terres cuites, *Ann. Geophys.*, *5*(2), 99–136.

Neel, L. (1955), Some theoretical aspects of rock magnetism, *Adv. Phys.*, *4*, 191–243.

Newell, A. J., and R. T. Merrill (1998), The curling nucleation mode in a ferromagnetic cube, *J. Appl. Phys.*, *84*(8), 4394–4402.

Newell, A. J., and R. T. Merrill (1999), Single-domain critical sizes for coercivity and remanence, *J. Geophys. Res.*, *104*, 617–628.

Özdemir, Ö., and D. J. Dunlop (1997), Effect of crystal defects and internal stress on the domain structure and magnetic properties of magnetite, *J. Geophys. Res.*, *102*(B9), 20,211–20,224.

Pike, C., and A. Fernandez (1999), An investigation of magnetic reversal in submicron-scale CO dots using first order reversal curve diagrams, *J. Appl. Phys.*, *85*(9), 6668–6676.

Pike, C. R., A. P. Roberts, M. J. Dekkers, and K. L. Verosub (2001), An investigation of multi-domain hysteresis mechanisms using FORC diagrams, *Phys. Earth Planet. Inter.*, *126*, 11–25.

Reichmann, H. J., and S. D. Jacobsen (2004), High-pressure elasticity of a natural magnetite crystal, *Am. Mineral.*, *89*, 1061–1066.

Schabes, M., and H. N. Bertram (1988), Magnetization processes in ferromagnetic cubes, *J. Appl. Phys.*, *64*, 1347–1357.

Soffel, H. C. (1969), The origin of thermoremanent magnetization of two basalts containing homogenous single phase titanomagnetite, *Earth Planet. Sci. Lett.*, *7*, 201–208.

Stacey, F. D., and K. N. Wise (1967), Crystal dislocations and coercivity in fine grained magnetite, *Aust. J. Phys.*, *20*, 507–513.

Tang, M., W. Cai, G. Xu, and V. V. Bulatov (2006), A hybrid method for computing forces on curved dislocations intersecting free surfaces in three-dimensional dislocation dynamics, *Modell. Simul. Mater. Sci. Eng.*, *14*, 1139–1151.

Tauxe, L. (1993), Sedimentary records of relative paleointensity of the geomagnetic field: Theory and practice, *Rev. Geophys.*, *31*(3), 319–354.

Till, J. L., M. J. Jackson, and B. M. Moskowitz (2010), Remanence stability and magnetic fabric development in synthetic shear zones deformed at 500°C, *Geochem. Geophys. Geosyst.*, *11*, Q12Z21, doi:10.1029/2010GC003320.

Till, J. L., and B. Moskowitz (2013), Magnetite deformation mechanism maps for better prediction of strain partitioning, *Geophys. Res. Lett.*, *40*, 697–702, doi:10.1002/grl.50170.

Tric, E., J. P. Valet, P. Tucholka, M. Paterne, L. Labeyrie, F. Guichard, L. Tauxe, and M. Fontugne (1992), Paleointensity of the geomagnetic field during the last 80,000 years, *J. Geophys. Res.*, *97*(B6), 9337–9351.

Voyles, P. M., J. L. Grazul, and D. A. Muller (2003), Imaging individual atoms inside crystals with ADF-STEM, *Ultramicroscopy*, *96*, 251–273.

Witt, A., K. Fabian, and B. Ulrich (2005), Three-dimensional micromagnetic calculations for naturally shaped magnetite: Octahedra and magnetosomes, *Earth Planet. Sci. Lett.*, *223*, 311–324.

Worm, H. U., and H. Markert (1987), The preparation of dispersed titanomagnetite particles by the glass-ceramic method, *Phys. Earth Planet. Inter.*, *46*, 263–269.

Xu, S., and R. T. Merrill (1989), Microstress and microcoercivity in multidomain grains, *J. Geophys. Res.*, *94*(B8), 10,627–10,636.

Xu, S., and R. T. Merrill (1990), Microcoercivity, bulk coercivity and saturation remanence in multidomain materials, *J. Geophys. Res.*, *95*(B5), 7083–7090.

Xu, S., and R. T. Merrill (1992), Stress, grain size, and magnetic stability of magnetite, *J. Geophys. Res.*, *97*(B4), 4321–4329.

Zhang, Z. F., Z. G. Wang, and Z. M. Sun (2001), Evolution and micro structural characteristics of deformation bands in fatigued copper single crystals, *Acta Mater.*, *49*, 2875–2886.